

Communication

Experimental Realization of Reconfigurable Photonic Lattices in Coherent Rydberg Atomic Vapors

Shun Liang^{1,†}, Qingsong Yu^{1,†}, Xing Lei^{2,3}, Shaohuan Ning¹, Changbiao Li¹, Yanpeng Zhang¹
and Zhaoyang Zhang^{1,*}

- ¹ Key Laboratory for Physical Electronics and Devices of the Ministry of Education & Shaanxi Key Lab of information Photonic Technique, School of Electronic Science and Engineering, Faculty of Electronic and Information Engineering, Xi'an Jiaotong University, Xi'an 710049, China; liangshun0606@stu.xjtu.edu.cn (S.L.); yuqingsong@stu.xjtu.edu.cn (Q.Y.); shaohuan0301@stu.xjtu.edu.cn (S.N.); cbli@mail.xjtu.edu.cn (C.L.); ypzhang@mail.xjtu.edu.cn (Y.Z.)
- ² National Key Laboratory of Science and Technology in Aircraft Control, Xi'an 710065, China; lx30@facri.com
- ³ Flight Automatic Control Research Institute, Xi'an 710065, China
- * Correspondence: zhyzhang@xjtu.edu.cn
- † These authors contributed equally to this work.

Abstract: We experimentally demonstrated the formation of a one-dimensional electromagnetically induced optical lattice in coherently prepared three-level ⁸⁵Rb Rydberg atomic vapors with electromagnetically induced transparency (EIT). The one-dimensional photonic lattice was optically induced by a coupling field with a spatially periodical intensity distribution deriving from the interference of two strong Gaussian beams from the same laser source (~480 nm). Under the Rydberg-EIT condition, the incident weak probe beam can feel a tunable spatially modulated susceptibility, which is verified by the controllable discrete diffraction pattern observed at the output plane of the vapor cell. This investigation not only opens the door for experimentally introducing the strong interaction between Rydberg atoms to govern the beam dynamics in photonic lattices based on atomic coherence but also provides an easily accessible periodic environment for exploring Rydberg-atom physics and related applications.

Keywords: photonic lattice; electromagnetically induced transparency; Rydberg atoms



Citation: Liang, S.; Yu, Q.; Lei, X.; Ning, S.; Li, C.; Zhang, Y.; Zhang, Z. Experimental Realization of Reconfigurable Photonic Lattices in Coherent Rydberg Atomic Vapors. *Photonics* **2022**, *9*, 422. <https://doi.org/10.3390/photonics9060422>

Received: 13 May 2022
Accepted: 14 June 2022
Published: 16 June 2022

Publisher's Note: MDPI stays neutral with regard to jurisdictional claims in published maps and institutional affiliations.



Copyright: © 2022 by the authors. Licensee MDPI, Basel, Switzerland. This article is an open access article distributed under the terms and conditions of the Creative Commons Attribution (CC BY) license (<https://creativecommons.org/licenses/by/4.0/>).

1. Introduction

Dating back to the last century, Rydberg atoms with valence electrons excited to highly lying energy levels were in the spotlight, helped by the development of high-resolution absorption spectroscopy [1]. Normally, Rydberg atoms manifest a long lifetime, large electric dipole moment, strongly enhanced interactions, large susceptibility, etc. [2]. Such exaggerated properties were employed for plenty of desired scientific research, including ultralong-range Rydberg molecules and Rydberg macro-dimer [3], single-photon applications [4,5], many-body physics [6], precision measurement [7], photon-photon interactions [8,9], and quantum information [10–12], to name a few.

By following the obtained remarkable achievements, the current belief is that it is essential to extend these superior features of Rydberg atoms to optical lattices [13], which can engineer the distribution of cold atoms into periodic manners. Such advantageous periodic frameworks have given rise to flourishing advancements in the study of hot topics in the physical community, including superpositions of macroscopically distinct states [14], dynamical crystal [15], single-atom-resolved interferometry [16], topological physics [17,18], and parity-time symmetry [19,20], among others. Very recently, two-dimensional Rydberg atom arrays have been constructed to demonstrate anti-blockaded effects [21] and quantum nonlinear optics [22]. The physical mechanism behind the emergence of fascinating effects in Rydberg atoms trapped by optical lattices can be attributed to the periodic modulation

of susceptibility arising from light-matter interactions. Such periodic susceptibility can lead to the formation of desired photonic band structures, which may play key roles in the generation of the aforementioned exotic properties, for example, topological photonics. In principle, exciting Rydberg atoms by a laser field with a spatially distributed intensity may also introduce periodicity into the susceptibility by utilizing atomic coherence such as electromagnetically induced transparency (EIT) in multi-level atomic systems [23,24].

Actually, optically induced photonic lattices [25–28] with instantaneously and in situ reconfigurability have been widely investigated by adopting EIT in lower-excited (e.g., $5S \leftrightarrow 5P$ or $5S \leftrightarrow 5D$ transitions) multi-level atomic configurations in recent years. Such electromagnetically induced photonic lattices are realized in both thermal and cold atomic settings [29,30] by patterning the refractive index profile in periodic manners with the assistance of EIT, which is driven by spatially structured coupling fields. Considering that EIT can effectively control the absorption, dispersion, and Kerr-type nonlinearity, electromagnetically induced optical lattices have been exploited to reveal a variety of phenomena, such as periodic Raman gain [31], edge solitons [32], all-optical tunable devices [33,34], non-Hermitian Talbot effect [35], and dynamics of vortices in the vicinity of Dirac points [36,37], that are not easily accessible in photonic lattices with fixed band structures. These previous works have paved the way for engineering periodic susceptibility with highly excited Rydberg states.

In this article, we construct a tunable one-dimension optically induced photonic lattice in a three-level ladder-type ^{85}Rb EIT configuration involving a Rydberg energy level. The Rydberg-state transition is accomplished by a weak Gaussian probe beam together with a strong coupling field. The coupling field is established by first splitting the output of a laser source into two identical beams and then interfering with them at the center of the ^{85}Rb vapor cell. As a result, the coupling field exhibits a one-dimension periodic stripe fringe along the x -direction. When the Gaussian probe field is launched into the coupling lattice along the opposite direction of the coupling field, a discrete diffraction pattern can be obtained at the output plane by adjusting the detuning of laser fields approaching the two-photon resonance, where a Rydberg-state EIT window occurs and leads to spatially periodic modulation on the refractive index of the sample. Furthermore, we explore the evolution of induced photonic lattices by observing the output diffraction patterns under different parametric regimes. A comprehensive theoretical simulation is also given to verify the experimental observations. Our work shows that atomic vapor can also provide a platform with periodicity to carry out investigations on the Rydberg atoms. This may open a new route to study the interactions between tunable band structures and properties of Rydberg excitations, potentially broadening related researches and applications.

2. Experimental Scheme

The experimental scheme is shown in Figure 1a. The optically induced photonic lattice is established in a three-level ladder-type configuration, composed of a ground state $5S_{1/2}(F=3)$, an intermediately-excited state $5P_{3/2}$, and a highly excited Rydberg state $37D_{5/2}$. A weak probe field (wavelength $\lambda_1 \approx 780.2$ nm) together with a strong coupling field ($\lambda_2 \approx 480$ nm) excites the valence electron to the Rydberg energy level. The experimental setup is provided in Figure 1b. The probe field E_1 (frequency ω_1 , horizontal polarization) emitted by a tunable external cavity diode laser (ECDL1, UniQuanta ECL801-780) is launched into a vapor cell filled with ^{85}Rb atoms along the z -axis to connect the transition $5S_{1/2} \rightarrow 5P_{3/2}$. The periodic coupling field E_2 with a structured intensity distribution (frequency ω_2 , vertical polarization, Rabi frequency Ω_2) is formed by interfering with two Gaussian coupling beams from the other ECDL2 (UniQuanta ECL801-480, with a maximum output power of ~ 240 mW) and counter-propagating with E_1 to drive the transition $5P_{3/2} \rightarrow 37D_{5/2}$. This counter-propagating arrangement of the two fields is designed to suppress the influence of Doppler broadening [23]. The two coupling beams are placed symmetrically with respect to the z -axis at an angle of $2\theta \approx 0.25^\circ$ and meet at center of the vapor cell to establish the standing-wave field with its periodicity (along the x -direction)

perpendicular to propagating direction. The periodic coupling field responsible for the modulation of the spatial refractive index is shown in Figure 1c, and its period along x is determined as $d = \lambda_2 / (2\sin\theta) \approx 110 \mu\text{m}$. The atomic vapor cell with a diameter of 2.5 cm and a length of 7 cm is packaged with μ -metal sheets (to shield the external magnetic field) and a heating tape. The heating system provides a temperature of 358 K, and the atomic density is $\sim 6.0 \times 10^{12} \text{ cm}^{-3}$.

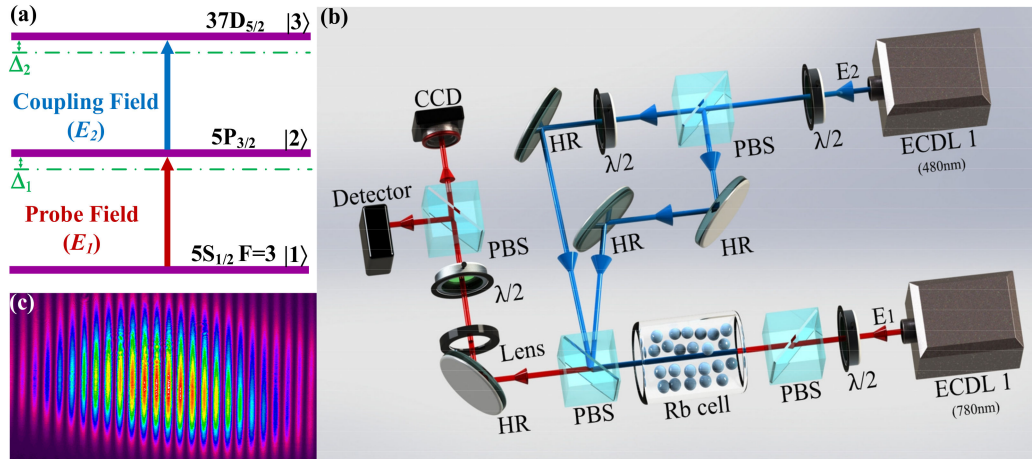


Figure 1. (a) The three-level ladder-type energy-level structure for excited Rydberg atoms. Both fields, E_1 and E_2 , are continuous waves. (b) Experimental setup. The vapor cell filled with ^{85}Rb atoms is heated to 348 K by a heating tape. The coupling laser beam from ECDL2 is split by a PBS and a half-wave plate into two identical parts, which intersect at the center of the vapor cell to form a standing wave. The horizontally polarized probe beam E_1 with the waist $w_0 \approx 800 \mu\text{m}$ from ECDL1 counter-propagates with the coupling field, and the transmitted probe is received by a CCD camera and a photoelectric detector. ECDL: external cavity diode laser; $\lambda/2$: half-wave plate; PBS: polarization beam splitter; CCD: charge-coupled-device camera; HR: high-reflectivity mirror. (c) The interference fringes of the two coupling beams.

With the frequency detuning set as $\Delta_1 = -100 \text{ MHz}$ relative to the resonant transition ($5S_{1/2} \rightarrow 5P_{3/2}$) driven by the probe field, it can experience substantial absorption. The presence of the coupling field can result in an EIT window when its detuning is adjusted to satisfying $\Delta_1 + \Delta_2 = 0$. Here, the frequency detuning Δ_1 (Δ_2) is defined as the difference between the laser frequency ω_1 (ω_2) and the energy gap of the two levels coupled by field E_1 (E_2) (see Figure 1a). The output probe field is divided into two parts by a PBS, and a small portion of the beam enters a photoelectric detector to monitor the EIT spectrum, while the rest part is received by a charge-coupled-device camera via an imaging lens, which guarantees the captured images are the beam profiles at the output plane of the vapor cell. Around the EIT window, one can observe clear diffraction patterns of the incident probe beam at the rear surface of the cell, indicating the formation of the spatially distributed refractive index.

3. Results

3.1. Theoretical Model

In theory, the spatial distribution of refractive index n depends on the intensity profile of the coupling lattice. By solving the density-matrix equations for the three-level atomic system under the rotating-wave approximation, the susceptibility χ of the Rydberg-EIT medium is $\chi = \chi' + \chi'' = (2N\mu_{21}/\epsilon_0 E_1)\rho_{21}$, where ϵ_0 is the permittivity of vacuum, N is the atomic density, μ_{21} and ρ_{21} are dipole moment and the density-matrix element for transition $5S_{1/2} \rightarrow 5P_{3/2}$, respectively, excited by the probe beam, and E_1 is the electrical-field intensity of the probe field. Term n can be written as $n = n_0 + \Delta n$ with $\Delta n = n_R + in_I$ (n_R and n_I are the real and imaginary parts of the refractive index, respectively). Considering $n_0 = 1$ is the

background index of the atomic gas, the modulation of the refractive index Δn caused by Rydberg EIT can be deduced as $\Delta n = n_R + in_I \approx \chi/2$, where $n_R \approx \chi'/2 = N\mu_{21}/\epsilon_0 E_1 \times \text{Re}(\rho_{21})$ and $n_I \approx \chi''/2 = N\mu_{21}/\epsilon_0 E_1 \times \text{Im}(\rho_{21})$. Even though the counter-propagating setting can partially suppress the Doppler effect, it cannot be neglected due to the relatively larger frequency difference $\omega_1 - \omega_2$. For an atom with a velocity of v , it feels an upshifted frequency of $\omega_1 v/c$ and a downshifted frequency of $\omega_2 v/c$ when it moves towards the probe and coupling beams, respectively. Consequently, the susceptibility with the Doppler effect taken into consideration can be expressed as [23,38]:

$$\chi(v)dv = \frac{i|\mu_{21}|^2/(\hbar\epsilon_0)}{\gamma_2 - i\Delta_1 - i\frac{\omega_1}{c}v + \frac{\Omega_2(x)^2/4}{\gamma_3 - i(\Delta_1 + \Delta_2) - i(\omega_1 - \omega_2)v/c}} N(v)dv, \tag{1}$$

where the spatially distributed Rabi frequency of the coupling field is defined as $\Omega_2(x) = \mu_{32}E_2/\hbar$ (μ_{32} is the dipole momentum for transition $5P_{3/2} \rightarrow 37D_{5/2}$, and E_2 is the electrical-field intensity of the coupling field) and then $\Omega_2(x)^2$ implies the intensity profile of the coupling lattice; \hbar is the reduced Planck constant; $N(v) = N_0 \exp(-v^2/u^2)/(u\pi^{1/2})$ is the particle number density in terms of speed distribution function with $u/2^{1/2}$ being the root-mean-square atomic velocity; the decay rate γ_i is natural widths of the intermediate $|2\rangle$ and upper states $|3\rangle$ ($i = 2, 3$); and c is the vacuum speed of light. Equation (1) describes the profile of susceptibility $\chi(v)$ by taking the spatial distribution of Rabi frequency $|\Omega_2(x)|^2$. With the Doppler effect considered, total susceptibility χ is obtained by the integration of $\chi(v)$ on the atomic velocity v :

$$\chi = \int_{-\infty}^{+\infty} \chi(v)dv. \tag{2}$$

Based on the total susceptibility χ in Equation (2), the theoretically calculated distributed real part $\text{Re}[\chi]$ of susceptibility can be obtained as Figure 2a,b when the probe field detuning is $\Delta_1 = -90$ MHz and $\Delta_1 = -110$ MHz, respectively, with $\Delta_2 = 100$ MHz. By comparing the two pictures with two-photon detuning $\delta = \Delta_1 + \Delta_2$ being 10 MHz and -10 MHz, one can see the distributions of the refractive index for the two cases exhibit difference, where the peak value on the index profile for $\delta = 10$ MHz corresponds to the valley value for $\delta = -10$ MHz. Namely, the change in the sign of the two-photon detuning can make the induced photonic lattice shift a half lattice period along the x -axis. Such a spatial movement coincides with the dispersion curve through the EIT window, where the refractive index can become larger or smaller than the background refractive index for the positive and negative sides of $\delta = 0$ [23]. Figure 2c,d depicts the imaginary part $\text{Im}[\chi]$ corresponding to Figure 2a,b, and one can see that $\text{Im}[\chi]$ is much smaller than the $\text{Re}[\chi]$ since the EIT can partially suppress the absorption. The spatial structure of the susceptibility regulated by two-photon detuning directly determines the output diffraction patterns of the probe beam. The probe dynamics inside such a discrete environment are governed by the Schrödinger-like paraxial propagation equation:

$$i\frac{\partial\psi(x,y,z)}{\partial z} = -\frac{1}{2k_1}\left(\frac{\partial^2}{\partial x^2} + \frac{\partial^2}{\partial y^2}\right)\psi + \frac{k_1}{n_0}\Delta n(x,y)\psi, \tag{3}$$

where ψ is the envelope of the incident probe beam, z is the propagation distance, and complex $\Delta n = n_R + in_I$ describes the periodic potential well “written” by the standing-wave coupling field under EIT. Figure 2e,f visually demonstrates the simulated output probe field passing through the atomic sample with a transversely discrete refractive index based on Equation (3) for the aforementioned two-photon detuning with opposite signs. The numerical results support that a weak Gaussian probe beam can be effectively discretized by the photonic lattices induced in a Rydberg-EIT atomic vapor. In addition to this, the output intensity profiles are also inversed (the positions of bright and dark fringes exchanged) for positive and negative two-photon detuning.

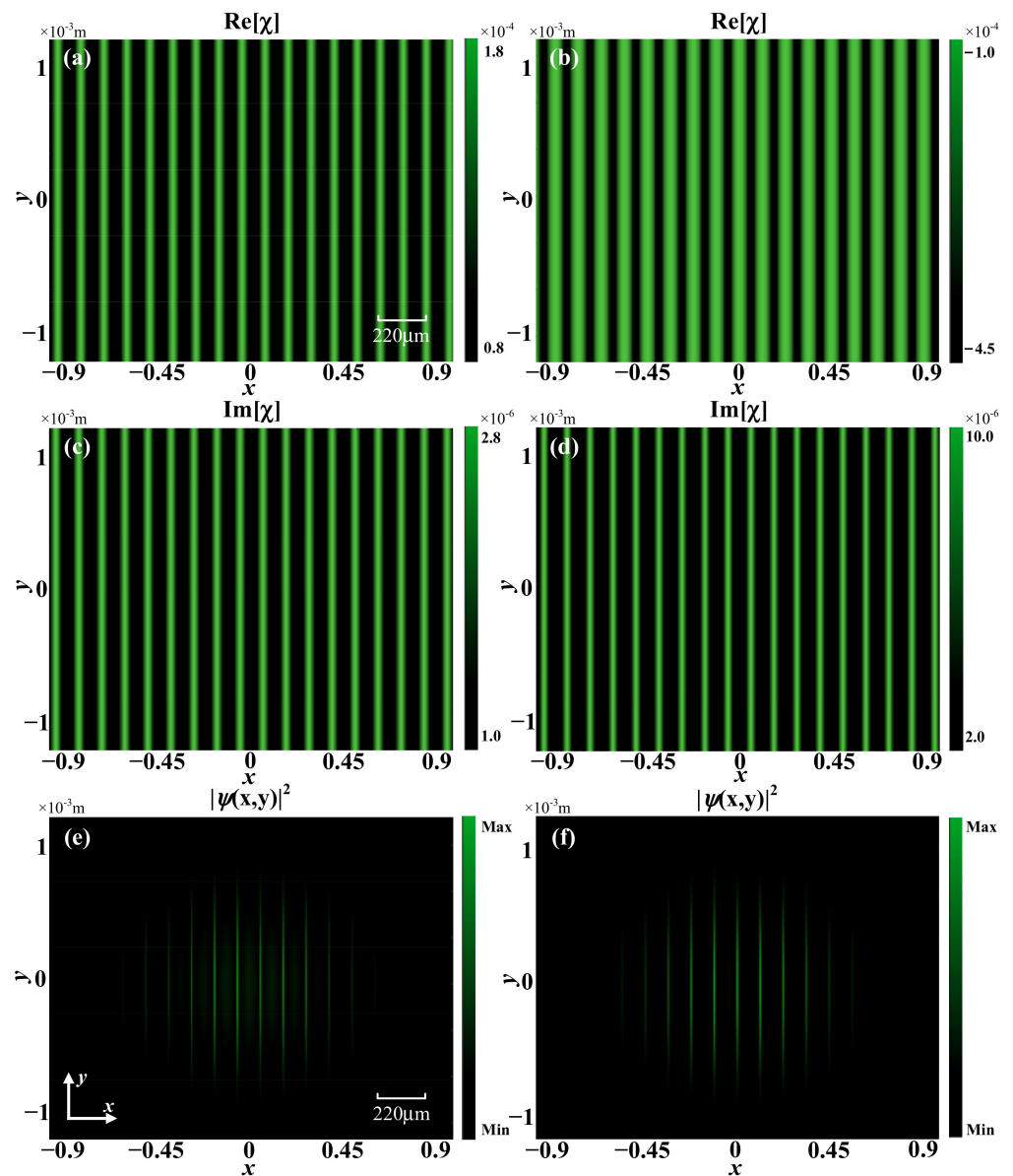


Figure 2. (a,b) The calculated susceptibility inside ^{85}Rb vapor cell at the probe-field detuning $\Delta_1 = -90$ MHz (a) and $\Delta_1 = -110$ MHz (b), respectively, with the coupling detuning fixed at $\Delta_2 = 100$ MHz. (c,d) The calculated imaginary parts of the susceptibility correspond to (a) and (b), respectively. (e,f) The theoretical output discrete diffraction patterns after the probe field traveling through the photonic lattice induced under the parametric conditions of (a,b). Parameters used in theoretical simulation: the atomic density $N = 6 \times 10^{12} \text{ cm}^{-3}$, the Rabi frequency of coupling field is $\Omega_2 = 2\pi \times 15.6$ MHz.

3.2. Experimental Results and Analysis on Manipulating Two-Photon Detuning

By experimentally setting the detuning of the coupling field at $\Delta_2 = 100$ MHz, the injected Gaussian probe field can demonstrate discrete dynamical behaviors with two-photon detuning $\delta = \Delta_1 - \Delta_2$ ranging from -30 MHz to 30 MHz. The structure of the induced photonic lattice, as well as the dynamics of the probe beam, can be manipulated by tuning the related experimental parameters due to the inherited reconfigurability from multi-level atomic systems. In the first place, the diffraction patterns of the probe beam exiting the Rydberg atomic vapor are provided in Figure 3 under different two-photon frequency detunings in the vicinity of the EIT window. Experimentally, such transmission images were captured by changing the probe detuning from -120 MHz to -70 MHz

but fixing the coupling-field detuning at $\Delta_2 = 100$ MHz. With the two-photon detuning δ evolving from -20 MHz to 0 , the contrast between the bright and dark fringes first becomes larger due to the increase of the modulation degree on the refractive index, and the highest contrast occurs around $\delta = -10$ MHz (Figure 3b); then, the difference between the intensity peak and valley becomes smaller, and there is almost no difference at $\delta = 0$ (Figure 3c). In the case of exact two-photon resonance, the probe field exhibits Gaussian distribution without any diffraction phenomena due to the disappeared modulation on the refractive index. Furthermore, the brightest pattern can be observed in this detuning point with the minimum absorption, where the imaginary part of the refractive index can be 0 in theory. It is worth noting that a very indistinct periodic intensity distribution can be observed because of the finite linewidth (~ 1 MHz) of the output from the adopted ECDLs. For the positive side of the two-photon resonance, the observed discretized patterns evolve similarly, with δ gradually adjusted near to the resonance.

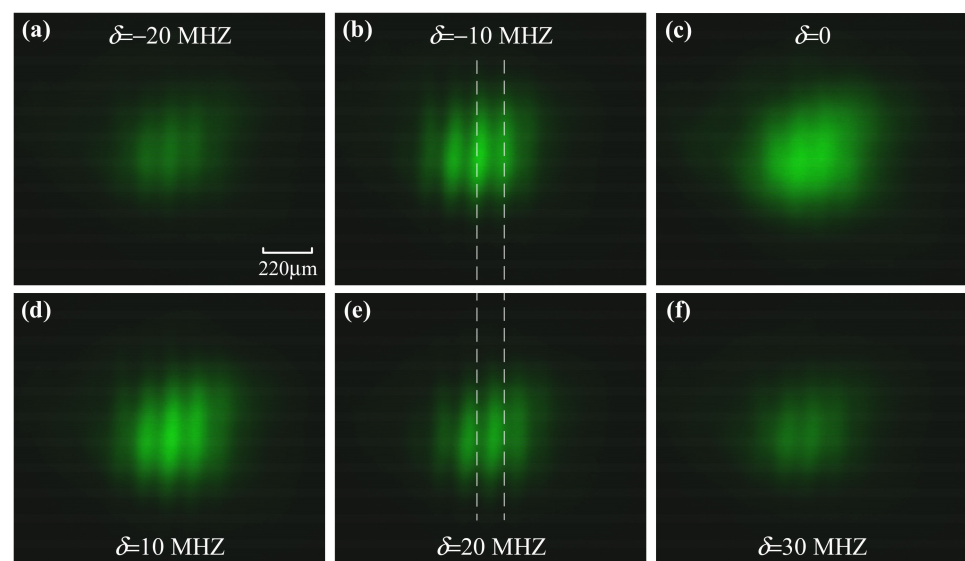


Figure 3. Observed intensity distributions of the output probe field for the different two-photon detuning $\delta = \Delta_1 - \Delta_2$ with coupling detuning Δ_2 being constantly 100 MHz. The powers of the probe and coupling field are 0.12 mW and 240 mW, respectively.

The overall evolutions of the diffraction patterns on either side of the two-photon resonance are governed by the change of the spatially distributed susceptibility, which is in accordance with the dispersion curve of a typical EIT medium [39]. Further, the captured patterns for two-photon detuning being negative (Figure 3a,b) and positive (Figure 3d,f) possess the same period but a half-period shift of the intensity peak (bright fringes). By comparing the output at $\delta = -10$ MHz (Figure 3b) and $\delta = 10$ MHz (Figure 3d), one can see that the shift of the bright fringes advocated the prediction in theoretical Figure 2e,f.

3.3. Experimental Results and Analysis on Manipulating Coupling Power

In order to achieve high diffractive efficiency in an electromagnetically induced lattice, the constructive and destructive interference should be carefully elaborated to realize the demanding spatial distribution of Rabi frequency with enough difference between maximum and minimum values according to Equation (1). Here, the diffraction efficiency of the n th-order diffractive beam is defined as $\eta_n = I_n' / I_0$, where I_n' represents the intensity of a selected n th-order diffractive beam (when $n = 0$, I_n' represents the intensity of 0th-order diffraction beam) and I_0 is the intensity of the probe beam transmitting through vapor without periodical refractive index [33,40]. Considering the large dipole momentum of a Rydberg atom, its Rabi frequency can be much smaller compared to lower-excited atoms under the same pump power. In other words, the high-contrast distribution of

Rabi frequency in Rydberg atoms can be realized only for high enough coupling power. Figure 4 demonstrates the dependence of diffractive efficiency (reflected by the intensity contrast of the output patterns) of the launched probe beam on the power of the coupling lattice. The two-photon detuning is chosen as 10 MHz to ensure the maximum contrast of the diffraction patterns. Here, the power means the total power of the two identical coupling beams responsible for the generation of the standing-wave coupling field. With the growth of the coupling power, it is clear that the diffractive patterns become more obvious, indicating an effective enhancement of the contrast between the peak and valley of the refractive index as well as the Rabi frequency. A larger coupling-field Rabi frequency means the excitation from intermediate states to Rydberg states can be more efficient. According to the observations, a clear diffraction pattern occurs when the coupling power increases over 120 mW, which is much larger than the required ~ 30 mW for the similar ladder-type EIT system but with a lower excitation ($5P_{3/2} \rightarrow 5D_{5/2}$) [29]. With the power of the coupling field increased to 240 mW, the diffractive efficiencies reach the maximum with $\eta_0 \approx 20\%$, $\eta_1 \approx 16\%$, and $\eta_2 \approx 7\%$, corresponding to 0th-, +1st-, and +2nd-order diffraction beams, respectively.

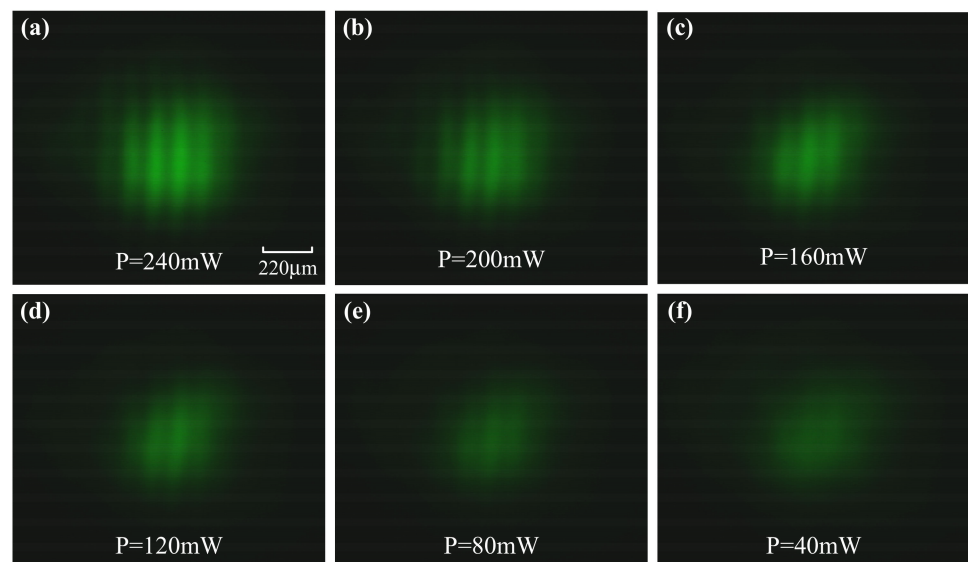


Figure 4. The output discrete diffraction of the probe field with the coupling-field power increased from 40 mW to 240 mW. The probe laser power is 0.12 mW, and the two-photon detuning $\delta = 10$ MHz with $\Delta_2 = 100$ MHz.

4. Discussion and Conclusions

In the present work, we experimentally realized the establishment of a one-dimensional electromagnetically induced optical lattice (with its period along the x -axis) in a three-level ladder-type ^{85}Rb atomic vapor with a Rydberg excitation. The strong coupling field responsible for the periodic modulation of the refractive index counter-propagates with a weak probe field to reduce the influence of Doppler broadening, and thus a Rydberg EIT window occurs. At the output plane of the vapor cell, clear one-dimensional discrete diffraction patterns were observed near the two-photon resonance, supporting the formation of periodic susceptibility in such a thermal Rydberg-EIT atomic configuration. The dynamical evolution of diffraction patterns through manipulating experimental parameters indicates the easily accessible reconfigurability and controllability of the established photonic lattices. The unique property of the Rydberg-EIT-based photonic lattice is that the strong Rydberg-Rydberg interactions are introduced as an indispensable degree of freedom for manipulating the behaviors of light in periodic structures.

Compared to the optically induced photonic lattices based on EIT in lower-excited multi-level atoms, the introduction of strong Rydberg-Rydberg interactions [41] may be

promising for operating nonlinear regimes as well as a variety of interesting proposals in future experiments, such as nonlinear light diffraction [42], parity-time symmetry optics [19], nonlocal optical solitons [20], single light bullets [43], and spatiotemporal solitons [44]. However, the experimental demonstration of photonic lattices with strong nonlinearity is lacking. The current optically induced photonic lattice with giant nonlinearity [45] can certainly provide a fertile ground for exploring dynamical behaviors of lights dominated by nonlinearity in periodic structures. Furthermore, Rydberg atoms trapped in optical lattices have spawned flourishing achievements in demonstrating unique optical features [14–19] by taking advantage of the interactions between Rydberg atoms and periodic environments. The currently demonstrated electromagnetically induced photonic lattice in coherently prepared atomic vapors, which possesses controllable Rydberg–Rydberg interactions and periodicity simultaneously but avoids the sophisticated laser-cooling equipment for trapping atoms into optical lattices, may pave the way to study the interactions between Rydberg atoms and periodicity in room temperature.

Author Contributions: Conceptualization, Z.Z.; methodology, Z.Z., X.L. and S.L.; software, S.L. and C.L.; validation, Z.Z. and Y.Z.; formal analysis, Z.Z., S.L. and X.L.; investigation, Z.Z., S.L. and Q.Y.; experiment, S.L., Q.Y. and S.N.; resources, Z.Z.; data curation, Q.Y.; writing—original draft preparation, S.L. and Q.Y.; writing—review and editing, S.L., Q.Y. and Z.Z.; visualization, S.L.; supervision, Z.Z. and Y.Z.; project administration, Z.Z.; funding acquisition, Z.Z. All authors have read and agreed to the published version of the manuscript.

Funding: This research was funded by the National Key R&D Program of China (2018YFA0307500, 2017YFA0303703), the National Natural Science Foundation of China (62022066, 12074306, 11804267), and the Key Scientific and Technological Innovation Team of Shaanxi Province (2021TD-56).

Institutional Review Board Statement: Not applicable.

Informed Consent Statement: Not applicable.

Data Availability Statement: Data underlying the results presented in this paper are not publicly available at this time but may be obtained from the authors upon reasonable request.

Acknowledgments: The authors acknowledge helpful discussions with Liu Yang.

Conflicts of Interest: The authors declare no conflict of interest.

References

1. Lim, J.; Lee, H.; Ahn, J. Review of cold Rydberg atoms and their applications. *J. Korean Phys. Soc.* **2013**, *63*, 867–876. [[CrossRef](#)]
2. Gallagher, T.F. *Rydberg Atoms*; Cambridge University: Cambridge, UK, 1994.
3. Shaffer, J.P.; Rittenhouse, S.T.; Sadeghpour, H.R. Ultracold Rydberg molecules. *Nat. Commun.* **2018**, *9*, 1965. [[CrossRef](#)] [[PubMed](#)]
4. Dudin, Y.O.; Kuzmich, A. Strongly interacting Rydberg excitations of a cold atomic gas. *Science* **2012**, *336*, 887–889. [[CrossRef](#)] [[PubMed](#)]
5. Huber, B.; Baluksian, T.; Schlagmuller, M.; Kolle, A.; Kubler, H.; Low, R.; Pfau, T. GHz Rabi flopping to Rydberg states in hot atomic vapor cells. *Phys. Rev. Lett.* **2011**, *107*, 243001. [[CrossRef](#)]
6. Browaeys, A.; Lahaye, T. Many-body physics with individually controlled Rydberg atoms. *Nat. Phys.* **2020**, *16*, 132–142. [[CrossRef](#)]
7. Jing, M.; Hu, Y.; Ma, J.; Zhang, H.; Zhang, L.; Xiao, L.; Jia, S. Atomic superheterodyne receiver based on microwave-dressed Rydberg spectroscopy. *Nat. Phys.* **2020**, *16*, 911–915. [[CrossRef](#)]
8. Gorshkov, A.V.; Otterbach, J.; Fleischhauer, M.; Pohl, T.; Lukin, M.D. Photon-photon interactions via Rydberg blockade. *Phys. Rev. Lett.* **2011**, *107*, 133602. [[CrossRef](#)]
9. Yang, L.; He, B.; Wu, J.; Zhang, Z.; Xiao, M. Interacting photon pulses in a Rydberg medium. *Optica* **2016**, *3*, 1095–1103. [[CrossRef](#)]
10. Spring, J.B.; Metcalf, B.J.; Humphreys, P.C.; Kolthammer, W.S.; Jin, X.; Barbieri, M.; Datta, A.; Thomas-Peter, N.; Langford, N.K.; Kundys, D.; et al. Boson sampling on a photonic chip. *Science* **2013**, *339*, 798–801. [[CrossRef](#)]
11. Levine, H.; Keesling, A.; Omran, A.; Bernien, H.; Schwartz, S.; Zibrov, A.S.; Endres, M.; Greiner, M.; Vuletic, V.; Lukin, M.D. High-fidelity control and entanglement of Rydberg-atom qubits. *Phys. Rev. Lett.* **2018**, *121*, 123603. [[CrossRef](#)]
12. Saffman, M.; Walker, T.G.; Mølmer, K. Quantum information with Rydberg atoms. *Rev. Mod. Phys.* **2010**, *82*, 2313. [[CrossRef](#)]
13. Anderson, S.E.; Younge, K.C.; Raithe, G. Trapping Rydberg atoms in an optical lattice. *Phys. Rev. Lett.* **2011**, *107*, 263001. [[CrossRef](#)] [[PubMed](#)]
14. Omran, A.; Levine, H.; Keesling, A.; Semeghini, G.; Wang, T.; Ebadi, S.; Bernien, H.; Zibrov, A.S.; Pichler, H.; Choi, S.; et al. Generation and manipulation of Schrödinger cat states in Rydberg atom arrays. *Science* **2019**, *365*, 570–574. [[CrossRef](#)] [[PubMed](#)]

15. Schachenmayer, J.; Lesanovsky, I.; Micheli, A.; Daley, A.J. Dynamical crystal creation with polar molecules or Rydberg atoms in optical lattices. *New J. Phys.* **2010**, *12*, 103044. [[CrossRef](#)]
16. Zeiher, J.; Bijnen, R.; Schauss, P.; Hild, S.; Choi, J.Y.; Pohl, T.; Bloch, I.; Gross, C. Many-body interferometry of a Rydberg-dressed spin lattice. *Nat. Phys.* **2016**, *12*, 1095–1099. [[CrossRef](#)]
17. De Léséleuc, S.; Lienhard, V.; Scholl, P.; Barredo, D.; Weber, S.; Lang, N.; Buchler, H.; Lahaye, T.; Browaeys, A. Observation of a symmetry-protected topological phase of interacting bosons with Rydberg atoms. *Science* **2019**, *365*, 775–780. [[CrossRef](#)]
18. Kanungo, S.K.; Whalen, J.D.; Lu, Y.; Yuan, M.; Dasgupta, S.; Dunning, F.B.; Hazzard, K.R.A.; Killian, T.C. Realizing topological edge states with Rydberg-atom synthetic dimensions. *Nat. Commun.* **2022**, *13*, 972. [[CrossRef](#)]
19. Xu, S.; Li, H.; Qin, Z.; Zhou, G.; Belic, M.; He, J.; Zhao, Y.; Zhao, D. Parity-time symmetry light bullets in a cold Rydberg atomic gas. *Opt. Express* **2020**, *28*, 16322–16332. [[CrossRef](#)]
20. Hang, C.; Huang, G. Parity-time symmetry along with nonlocal optical solitons and their active controls in a Rydberg atomic gas. *Phys. Rev. A* **2018**, *98*, 043840. [[CrossRef](#)]
21. Liu, F.; Yang, Z.; Bienias, P.; Iadecola, T.; Gorshkov, A.V. Localization and criticality in antiblockaded two-dimensional Rydberg atom arrays. *Phys. Rev. Lett.* **2022**, *128*, 013603. [[CrossRef](#)]
22. Moreno-Cardoner, M.; Goncalves, D.; Chang, D.E. Quantum nonlinear optics based on two-dimensional Rydberg atom arrays. *Phys. Rev. Lett.* **2021**, *127*, 263602. [[CrossRef](#)] [[PubMed](#)]
23. Geabanacloche, J.; Li, Y.; Jin, S.; Xiao, M. Electromagnetically induced transparency in ladder-type inhomogeneously broadened media: Theory and experiment. *Phys. Rev. A* **1995**, *51*, 576. [[CrossRef](#)] [[PubMed](#)]
24. Petrosyan, D.; Otterbach, J.; Fleischhauer, M. Electromagnetically induced transparency with Rydberg atoms. *Phys. Rev. Lett.* **2011**, *107*, 213601. [[CrossRef](#)] [[PubMed](#)]
25. Ning, S.; Lu, J.; Liang, S.; Feng, Y.; Li, C.; Zhang, Z.; Zhang, Y. Talbot effect of an electromagnetically induced square photonic lattice assisted by a spatial light modulator. *Opt. Lett.* **2021**, *46*, 5035–5038. [[CrossRef](#)]
26. Yuan, J.; Wu, C.; Wang, L.; Chen, G.; Jia, S. Observation of diffraction pattern in two-dimensional optically induced atomic lattice. *Opt. Lett.* **2019**, *44*, 4123–4126. [[CrossRef](#)]
27. Zhang, Z.; Shen, Y.; Ning, S.; Liang, S.; Feng, Y.; Li, C.; Zhang, Y.; Xiao, M. Transport of light in a moving photonic lattice via atomic coherence. *Opt. Lett.* **2021**, *46*, 4096–4099. [[CrossRef](#)]
28. Chen, Z.; Liu, X.; Zeng, J. Electromagnetically induced moiré optical lattices in a coherent atomic gas. *Front. Phys.* **2022**, *17*, 42508. [[CrossRef](#)]
29. Sheng, J.; Wang, J.; Miri, M.A.; Christodoulides, D.N.; Xiao, M. Observation of discrete diffraction patterns in an optically induced lattice. *Opt. Express* **2015**, *23*, 19777–19782. [[CrossRef](#)]
30. Zhang, H.; Yuan, J.; Dong, S.; Wu, C.; Wang, L. Observation of an electromagnetically induced grating in cold ⁸⁵Rb atoms. *Appl. Sci.* **2020**, *10*, 5740. [[CrossRef](#)]
31. Zhang, Z.; Feng, J.; Liu, X.; Sheng, J.; Zhang, Y.; Zhang, Y.; Xiao, M. Controllable photonic crystal with periodic Raman gain in a coherent atomic medium. *Opt. Lett.* **2018**, *43*, 919–922. [[CrossRef](#)]
32. Zhang, Z.; Wang, R.; Zhang, Y.; Kartashov, Y.; Li, F.; Zhong, H.; Guan, H.; Gao, K.; Li, F.; Zhang, Y.; et al. Observation of Edge Solitons in Photonic Graphene. *Nat. Commun.* **2020**, *11*, 1902. [[CrossRef](#)] [[PubMed](#)]
33. Zhang, H.; Yuan, J.; Dong, S.; Wu, C.; Wang, L.; Xiao, L.; Jia, S. All-optical tunable high-order Gaussian beam splitter based on a periodic dielectric atomic structure. *Opt. Express* **2021**, *29*, 25439–25448. [[CrossRef](#)] [[PubMed](#)]
34. Yuan, J.; Dong, S.; Zhang, H.; Wu, C.; Wang, L.; Xiao, L.; Jia, S. Efficient all-optical modulator based on a periodic dielectric atomic lattice. *Opt. Express* **2021**, *29*, 2712–2719. [[CrossRef](#)]
35. Zhang, Z.; Feng, Y.; Ning, S.; Malpuech, G.; Solnyshkov, D.; Xu, Z.; Zhang, Y.; Xiao, M. Imaging lattice switching with Talbot effect in reconfigurable non-Hermitian photonic graphene. *Photon. Res.* **2022**, *10*, 958–964. [[CrossRef](#)]
36. Zhang, Z.; Liang, S.; Li, F.; Ning, S.; Li, Y.; Guillaume, M.; Zhang, Y.; Xiao, M.; Solnyshkov, D. Spin-orbit coupling in photonic graphene. *Optica* **2020**, *7*, 455–462. [[CrossRef](#)]
37. Zhang, Z.; Li, F.; Malpuech, G.; Zhang, Y.; Bleu, O.; Koniakhin, S.; Li, C.; Zhang, Y.; Xiao, M.; Solnyshkov, D. Particle-like behavior of topological defects in linear wave packets in photonic graphene. *Phys. Rev. Lett.* **2019**, *122*, 233905. [[CrossRef](#)]
38. Mohapatra, A.K.; Jackson, T.R.; Adams, C.S. Coherent optical detection of highly excited Rydberg states using electromagnetically induced transparency. *Phys. Rev. Lett.* **2007**, *98*, 113003. [[CrossRef](#)]
39. Xiao, M.; Li, Y.; Jin, S.; Gea-Banacloche, J. Measurement of dispersive properties of electromagnetically induced transparency in rubidium atoms. *Phys. Rev. Lett.* **1995**, *74*, 666–669. [[CrossRef](#)]
40. Yuan, J.; Dong, S.; Wu, C.; Wang, L.; Xiao, L.; Jia, S. Optically tunable grating in a V+ $\bar{\Sigma}$ configuration involving a Rydberg state. *Opt. Express* **2020**, *28*, 23820–23828. [[CrossRef](#)]
41. Chen, C.; Yang, F.; Wu, X.; Shen, C.; Tey, M.K.; You, L. Two-color optical nonlinearity in an ultracold Rydberg atom gas mixture. *Phys. Rev. A* **2021**, *103*, 053303. [[CrossRef](#)]
42. Hang, C.; Li, W.; Huang, G. Nonlinear light diffraction by electromagnetically induced gratings with PT symmetry in a Rydberg atomic gas. *Phys. Rev. A* **2019**, *100*, 043807. [[CrossRef](#)]
43. Bai, Z.; Li, W.; Huang, G. Stable single light bullets and vortices and their active control in cold Rydberg gases. *Optica* **2019**, *6*, 309–317. [[CrossRef](#)]

-
44. Xu, S.; Zhou, Q.; Zhao, D.; Belic, M.; Zhao, Y. Spatiotemporal solitons in cold Rydberg atomic gases with Bessel optical lattices. *Appl. Math. Lett.* **2020**, *106*, 106230. [[CrossRef](#)]
 45. Walther, V.; Johne, R.; Pohl, T. Giant optical nonlinearities from Rydberg excitons in semiconductor microcavities. *Nat. Commun.* **2018**, *9*, 1309. [[CrossRef](#)] [[PubMed](#)]